

Electrochemical feedback on strain dynamics in noble metal nanocatalysts

Raphael Chattot (✉ raphael.chattot@grenoble-inp.org)

European Synchrotron Radiation Facility <https://orcid.org/0000-0001-6169-530X>

Isaac Martens

European Synchrotron Radiation Facility

Marta Mirolo

European Synchrotron Radiation Facility

Michal Ronovsky

European Synchrotron Radiation Facility

Florian Russello

European Synchrotron Radiation Facility

Helena Isern

European Synchrotron Radiation Facility

Guillaume Braesch

CNRS

Elisabeth Hornberger

Technische Universität Berlin <https://orcid.org/0000-0003-4548-8911>

Peter Strasser

Technical University of Berlin <https://orcid.org/0000-0002-3884-436X>

Eric Sibert

CNRS

Marian Chatenet

Grenoble Institute of Technology <https://orcid.org/0000-0002-9673-4775>

Veijo Honkimaki

European Synchrotron Radiation Facility

Jakub Dmec

European Synchrotron Radiation Facility

Article

Keywords: noble metal nanocatalysts, electrocatalysis, nanoparticles, fuel cells

Posted Date: March 19th, 2021

DOI: <https://doi.org/10.21203/rs.3.rs-315246/v1>

License:  This work is licensed under a Creative Commons Attribution 4.0 International License.

[Read Full License](#)

Electrochemical feedback on strain dynamics in noble metal nanocatalysts

Raphaël Chattot^{1,}, Isaac Martens¹, Marta Mirolo¹, Michal Ronovsky¹, Florian Russello¹, Helena Isern
Herrera¹, Guillaume Braesch², Elisabeth Hornberger³, Peter Strasser³, Eric Sibert², Marian Chatenet²,
Veijo Honkimäki¹, and Jakub Drnec¹*

¹ European Synchrotron Radiation Facility, ID 31 Beamline, BP 220, F-38043 Grenoble, France

² Univ. Grenoble Alpes, Univ. Savoie Mont Blanc, CNRS, Grenoble INP*, LEPMI, 38000 Grenoble,
France. *Institute of Engineering and Management Univ. Grenoble Alpes

³ Electrochemical Energy, Catalysis and Material Science Laboratory, Department of Chemistry,
Technische Universität Berlin, 10623 Berlin, Germany

*e-mail: (RC) raphael.chattot@grenoble-inp.org

1 **Abstract**

2 The theoretical design of effective metal electrocatalysts for energy conversion and storage devices relies
3 on the structure sensitivity of electrochemical processes to their catalyst materials, assuming the structural
4 integrity during operation. However, theoretical predictions do not necessarily match practical
5 performance. Here, by using high-energy X-ray diffraction from the new Extremely Brilliant Source of the
6 European Radiation Synchrotron Facility (ESRF-EBS) on device-relevant Pd and Pt nanocatalysts during
7 cyclic voltammetry experiments in liquid electrolyte, we quantitatively reveal how different
8 electrochemical processes permanently affect the bulk microstructure of nanocatalysts in a distinctive
9 fashion. The reported structural insights provide experimental access to reactivity descriptors such as
10 adsorption and absorption trends *operando*. The ease and power of such an experimental approach at new
11 and future beamlines is foreseen to guide computational model description of practical nanomaterials in
12 electrochemical environment while providing a discovery platform toward the study of nanocatalysts
13 encompassing a large variety of applications.

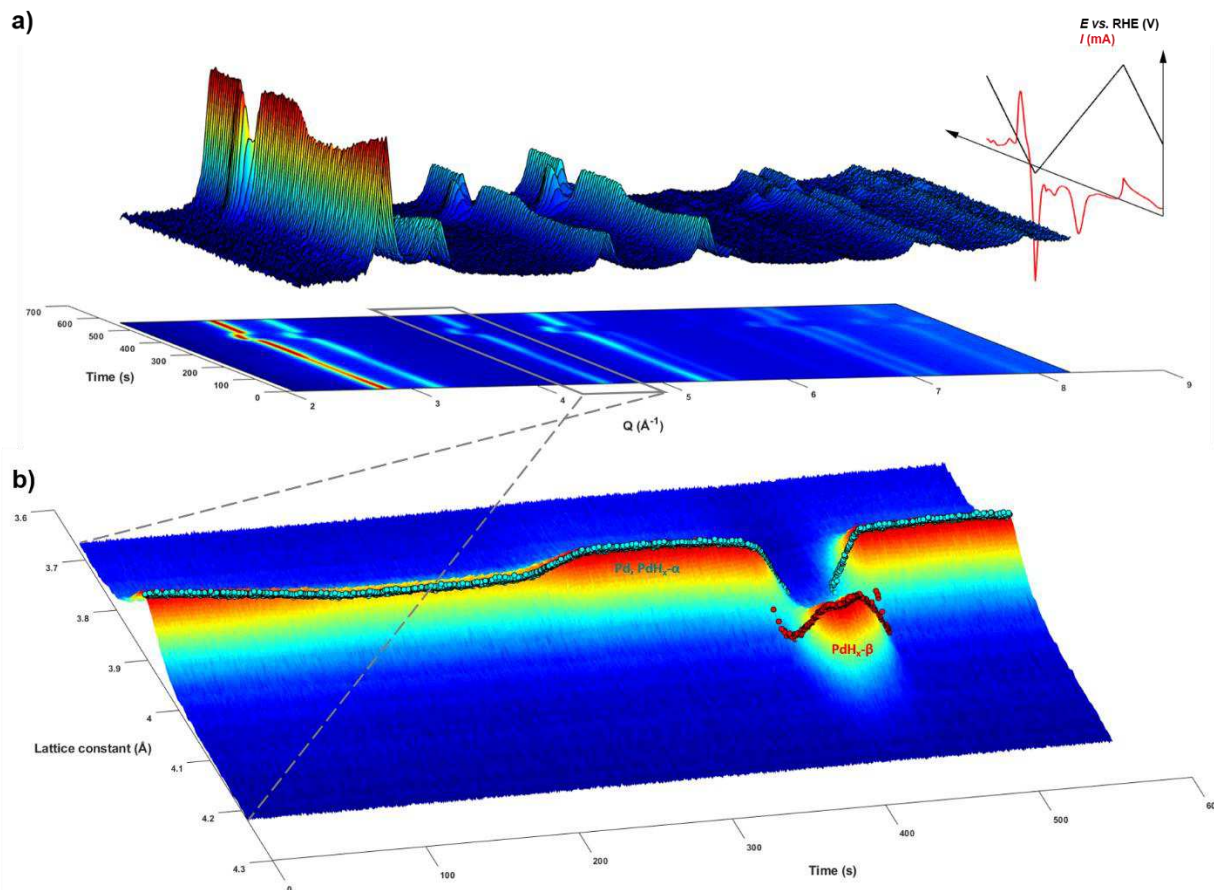
15 **Text**

16 Surface science has driven the development of commercial nanocatalysts for energy conversion and storage
17 applications, by establishing the electronic descriptors that rationalize or even predict the activity of metallic
18 surfaces for numerous reactions in the frame of the Sabatier principle: the ability of the surface to bind
19 adsorbates and the strength of the bonds define the reaction thermodynamics and kinetics¹⁻⁵. This seminal
20 knowledge has allowed tremendous improvements in electrocatalytic materials according to the ‘catalysts-
21 by-design’⁶ approach, where catalytic performance is tailored by the surface crystallographic structure and
22 chemical composition⁷⁻⁹. However, there are discrepancies between the predicted and practical
23 performances of nanomaterials¹⁰. These discrepancies arise from fundamental differences between single
24 crystals and nanoparticles surface geometries¹¹, also with the drastic changes of (surface) chemistry of

1 nanocatalyst materials observed during electrochemical operation ¹²⁻¹⁵. Numerous approaches are explored
2 to bridge catalytic surface physico-chemical state dynamics during operation and its interaction with
3 electrochemical species ¹⁶. Among them, photon-based techniques, *e.g.* surface X-ray diffraction and
4 spectroscopic methods have been extensively employed for palladium (Pd) ¹⁷⁻²² and platinum (Pt) ²³⁻³²,
5 which play a central role in fuel cells electrocatalysis. Still, due to the techniques' inherent limitations, most
6 studies are conducted on model systems such as extended single-crystals, shape- or size-controlled large
7 (20-50 nm) nanoparticles, in unrealistic sample environments or with rather low temporal and/or potential
8 resolution. Therefore, methods allowing the experimental determination of electrochemical adsorption
9 trends on practical catalytic materials during operation are urgently needed to close the gap between theory
10 and application.

11 In this contribution, we use the light from the new 4th generation Extremely Brilliant Source of the European
12 Radiation Synchrotron Facility (ESRF-EBS, Grenoble, France) to investigate the structural evolution of
13 device-relevant, carbon-supported Pd and Pt nanocatalysts during cyclic voltammetry experiments in liquid
14 electrolyte. The brilliance and high-energy of the employed X-rays transpose to a new level of
15 microstructural information combined quality and temporal resolution for *operando* measurements. Our
16 results firstly reveal that the bulk microstructure of carbon-supported Pd (Pd/C) and Pt (Pt/C) nanoparticles
17 in such conditions is controlled by the electrochemical environment, and differ from the *ex-situ* state. The
18 degree of modification not only depends on electrode potential but also on electrode history. For Pd, the
19 reported structural changes provide new insights in the mechanism of electroabsorbed hydrogen-induced
20 phase transition, notably by capturing the transient core-shell mechanism involving supersaturated and
21 undersaturated hydrogenated phases. Further comparison between Pd and Pt structural evolutions in relation
22 with their respective cyclic voltammograms establishes direct linear relation between the nanoparticles bulk
23 lattice constants and adsorbates surface coverage. These experimental results should serve computational
24 models improving nanocatalysts' description in electrochemical environment while providing versatile
25 experimental access to reactivity descriptors on practical nanocatalysts *operando*.

1



2

3 **Figure 1.** New light on Pd nanoparticles during cyclic voltammetry. a) 3D representation and corresponding
 4 2D projection of WAXS patterns intensities (I over 20) plotted as a function of time and the momentum transfer
 5 Q recorded during Pd cyclic voltammetry experiment in N_2 -purged 0.1 M NaOH electrolyte at room
 6 temperature. The evolutions of the electrochemical potential applied and measured electric current are also
 7 represented on the same time scale; b) surface plot focus on a narrow Q window showing the full time resolution
 8 evolution of the two phases (Pd, or $\text{PdH}_x\text{-}\alpha$ and $\text{PdH}_x\text{-}\beta$) [220] reflections. In b), the Q scale (left) is converted
 9 to the corresponding lattice constants, and the values calculated by Rietveld refinement of the full patterns are
 10 plotted on the surface of the plot. The exposure time for WAXS measurement was 250 ms, leading to an overall
 11 temporal resolution of 333 ms. The electrode was loaded with $1.45 \text{ mg}_{\text{metal}} \text{ cm}^{-2}$ and the sweep rate was 5 mV
 12 s^{-1} .

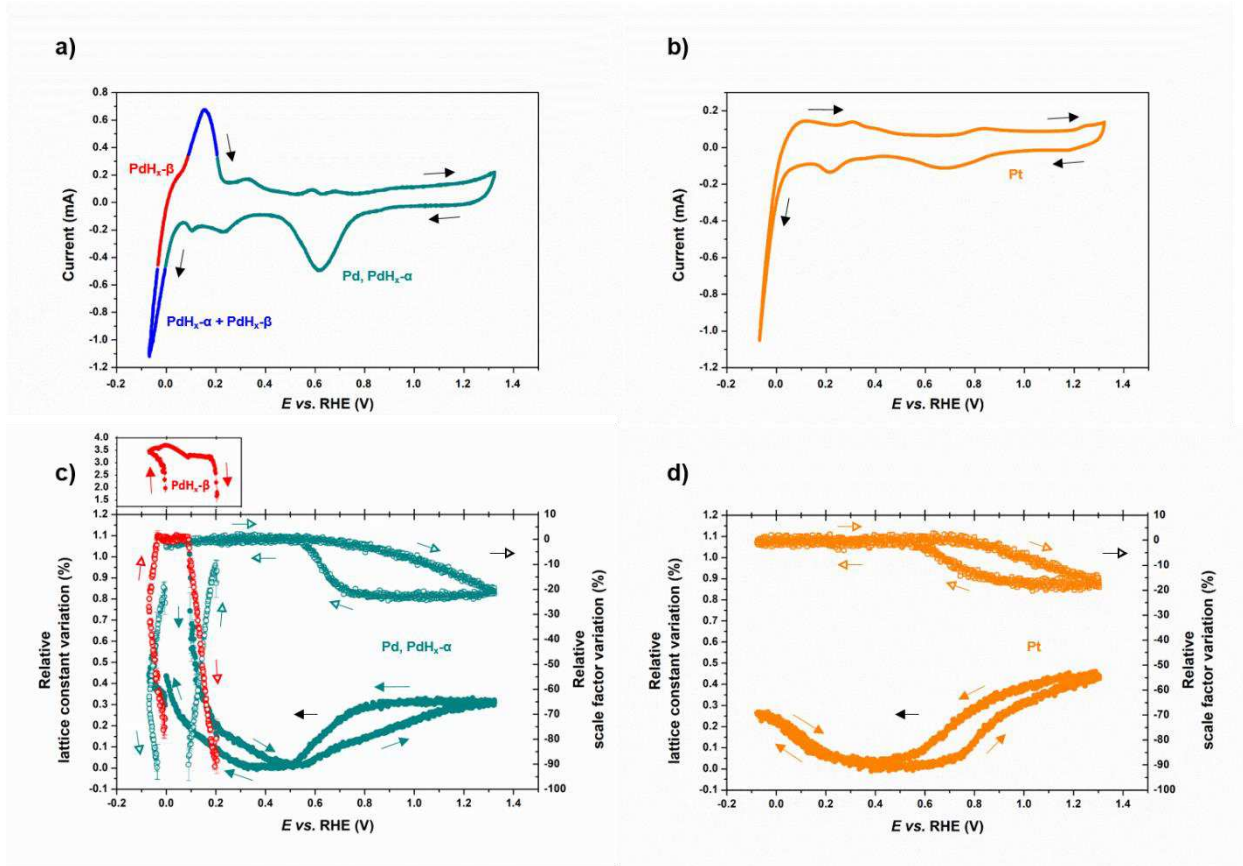
13 **Figure 1.a** shows a typical wide-angle X-ray scattering (WAXS) dataset obtained during cyclic
 14 voltammetry of Pd/C nanoparticles in N_2 -purged 0.1 M NaOH electrolyte at room temperature. When

1 probed with sufficiently bright and energetic X-rays (here $2 \cdot 10^{12}$ photons s^{-1} at 78 keV), the electrocatalytic
2 thin films ($1.45 \text{ mg}_{\text{metal}} \text{ cm}^{-2}$ or $25 \text{ } \mu\text{g}_{\text{metal}} \text{ cm}^{-2}$ for transmission or grazing incidence configurations,
3 respectively) contained in 3-electrode flow cells (**Figure S1** in Supplementary Information) produce very
4 low-noise signals on the detector in short exposure time (below 300 ms), which can then be further reduced
5 to high-quality diffraction patterns of high temporal resolution (below 400 ms). Analyzing the full patterns
6 with the Rietveld refinement method allows tracking the microstructure of the nanoparticles composing the
7 catalyst, *e.g.* crystal phase structure, lattice constant or coherent domain size from the WAXS reflections
8 position, intensity and shape (**Figure 1.b**). In addition, the scale factor (the Bragg peaks' area) relates to
9 the quantity of unit cells from the crystals contributing to the diffraction pattern.

10 Cyclic voltammograms (**Figure 2.a** and **2b** for Pd/C and Pt/C, respectively) show the usual features of these
11 noble metal electrodes, *e.g.* underpotential adsorption-absorption/desorption of hydrogen ($0.05 \leq E \leq 0.30$
12 V *vs.* RHE), adsorption/desorption of oxygenated species ($E \geq 0.50$ V *vs.* RHE) and hydrogen evolution
13 ($E < 0.05$ V *vs.* RHE). Strikingly, the relative variations of the lattice constants and scale factors (in %,
14 compared to their values measured in the double-layer region at $E = 0.5$ V *vs.* RHE), show near-permanent
15 dependency with the electrode potential and history (**Figure 2.c** and **2d** for Pd/C and Pt/C, respectively).
16 This suggests that the different electrochemical processes listed above produce important feedback on the
17 catalysts microstructures. Electrode polarization at high potential ($E > 0.5$ V *vs.* RHE) leads to $\sim 0.3\%$ and
18 0.4% lattice constant expansion for Pd/C and Pt/C, respectively, accompanied with $\sim 20\%$ scale factor losses
19 for the two materials. These changes are found irreversible with the applied potential, as pronounced
20 hysteresis are observed. For Pt, the trends agree with the pioneer work from Martens *et al.*, who used this
21 indicator to investigate Pt oxidation dynamics³². Although quantitatively different, the trends for both Pd
22 and Pt materials appear qualitatively similar at high potential. Electrode polarization at low potential ($E <$
23 0.4 V *vs.* RHE), however, leads to sharp differences in microstructural evolution. The latter mainly originate
24 from Pd's ability to absorb hydrogen compared to Pt. The PdH_x $\alpha \leftrightarrow \beta$ phase transitions during cyclic
25 voltammetry were clearly captured by the WAXS patterns (new set of reflections in **Figure 1**), and

1 transpose to two distinct lattice constants and scale factors (**Figure 2.c**). The Pd, or PdH_x- α phase
2 corresponds to Pd when no or few hydrogen atoms are inserted in octahedral interstitial positions and PdH_x-
3 β when further hydrogen atoms are inserted in octahedral interstitial positions. The regions corresponding
4 to the existence and co-existence of the different PdH_x phases revealed by their scale factors are indicated
5 in the colored cyclic voltammogram (**Figure 2.a**). Whereas **Figure 2.d** reveals that adsorption and
6 desorption of hydrogen produce rather reversible variation of Pt lattice constant and preserve the
7 nanoparticles coherence (constant and maximum scale factor), the phase transitions PdH_x $\alpha \leftrightarrow \beta$ appear
8 irreversible. However, such hysteresis in cyclic voltammetry experiment likely originates from combined
9 thermodynamically-irreversible processes³³ and slow kinetics. In the following, we first focus on the
10 microstructural modifications of Pd by electrochemical hydrogen absorption, before discussing the
11 complete picture of hydrogen and oxygenated species adsorption and/or absorption processes on both Pd
12 and Pt.

13



1
2 **Figure 2: High time resolution monitoring of nanocatalysts microstructures during cyclic voltammetry.** Cyclic
3 voltammogram of the (a) Pd/C and (b) Pt/C catalysts in N_2 -purged 0.1 M NaOH recorded at room temperature
4 with a potential sweep rate of 5 mV s^{-1} ; potential-dependency of the relative lattice constant variation (filled
5 symbols, left axis) and relative scale factor (Bragg peaks area) variation (hollow symbols, right axis for the (c)
6 Pd/C and (d) Pt/C catalysts. In a), the current recorded in the potential regions is colored in cyan when only the
7 phase Pd or $PdH_{x-\alpha}$ is detected, in red when only the $PdH_{x-\beta}$ is detected and in blue when both $PdH_{x-\alpha}$ and
8 $PdH_{x-\beta}$ are detected simultaneously. In c) the signal colored in cyan corresponds to the Pd or $PdH_{x-\alpha}$ phase and
9 the signal colored in red corresponds to the $PdH_{x-\beta}$ phase. For the sake of clarity, the relative lattice constant
10 variation of $PdH_{x-\beta}$ phase is represented in a separated plot with linked x-axis. In all panels, the signals are
11 displayed as scatter points (333 ms time resolution) and the error bars represent the standard deviation
12 associated with the refinement of the plotted parameters. The electrodes were loaded with $1.45 \text{ mg}_{\text{metal}} \text{ cm}^{-2}$
13 and measured in transmission configuration.

14

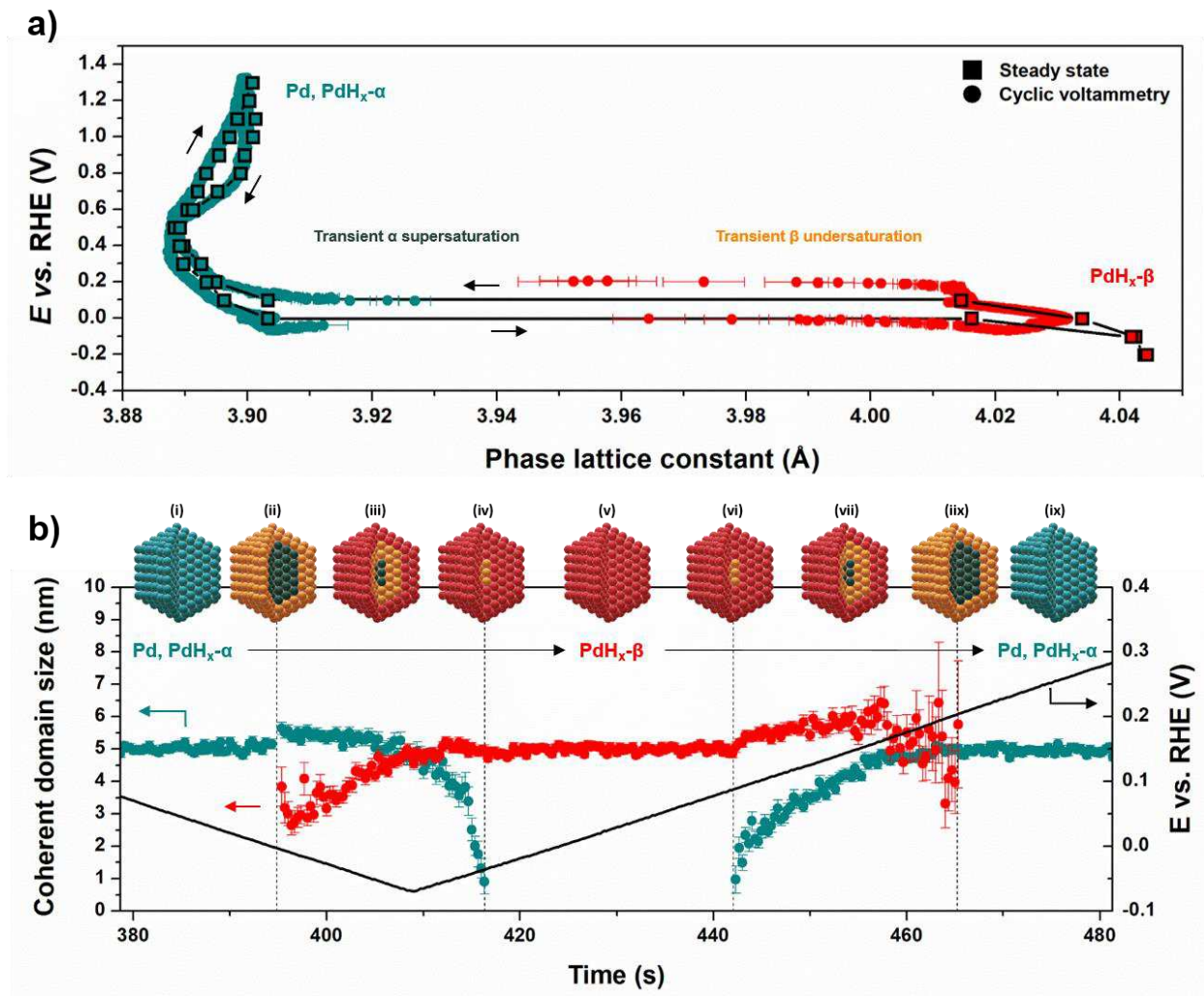
15

1 We strive to disentangle thermodynamics and kinetics aspects on the observed lattice constants hysteresis
2 during cyclic voltammetry, by showing Pd nanoparticles structural evolution during potential steps
3 experiment. Various intermediate quasi-steady states are captured by consecutive 60 s potential holds along
4 ascending and descending potential steps (staircase) of 100 mV (**Figure 3.a**). This potential hold duration
5 should exceed the overall longest transition time (35 s for the complete absorption) measured in a control
6 experiment (**Figure S2**). The as-obtained hysteresis plot (square symbols interpolated by black line and for
7 $E \leq 0.40$ V vs. RHE) recalls the apparent violation of the Gibbs phase rule observed in the classical hydrogen
8 pressure-composition isotherm for the Pd-H system in the gas phase ³⁴. In agreement with these former
9 results, hydride formation appears thermodynamically-disfavored, with here a value of at least 100 mV
10 overpotential compared to hydrogen desorption.

11 Superimposing the points recorded during cyclic voltammetry (circles) on the quasi-steady state plot
12 (**Figure 3.a**) reveals two significant features. The first is striking, continuous dynamics for both PdH_x- α
13 and PdH_x- β lattices observed during the PdH_x $\alpha \leftrightarrow \beta$ transitions. This challenges the commonly-accepted
14 concept of constant α_{\max} and β_{\min} (maximum/minimum insertion contents in the PdH_x- α and PdH_x- β phases,
15 respectively) during phase transition. The positions of both sets of reflections from XRD were reported
16 invariant during the two-phase regime by Eastman et al. ¹⁷ (α_{\max} of 3.9079 ± 0.002 Å and β_{\min} of $4.0167 \pm$
17 0.002 Å in the gas phase at room temperature), in total contradiction with the present observations during
18 the transients. One must note that very similar conclusions to Eastman's could have been reached here from
19 the lower time resolution dataset obtained at the quasi-steady state in **Figure 3.a**, which shows an apparent
20 α_{\max} of 3.9033 ± 0.0006 Å and β_{\min} of 4.0154 ± 0.002 Å. **Figure S3** shows selected WAXS patterns and
21 associated Rietveld fits capturing the [220] reflections angular shifts for both phases during phase-
22 transition. Our results support Lacher's idea introduced in 1937 ^{35,36} proposing the possibility of metastable
23 supersaturation of the PdH_x- α phase and undersaturation of the PdH_x- β phase during the transitions. This
24 transient phenomenon occurring at the interface of the two phases is also the cornerstone of the Schwarz
25 and Khachaturyan theory ^{37,38}, now generally accepted to account for the hysteresis. The second noticeable

1 feature concerns the ~ 100 mV positive overpotential difference of the $\text{PdH}_x \beta \rightarrow \alpha$ phase transition between
 2 steady state and cyclic voltammetry. This can be rationalized by slow hydrogen desorption kinetics that
 3 was reported to be both nanoparticle facet dependent³⁹ and alkali metal cation dependent⁴⁰.

4

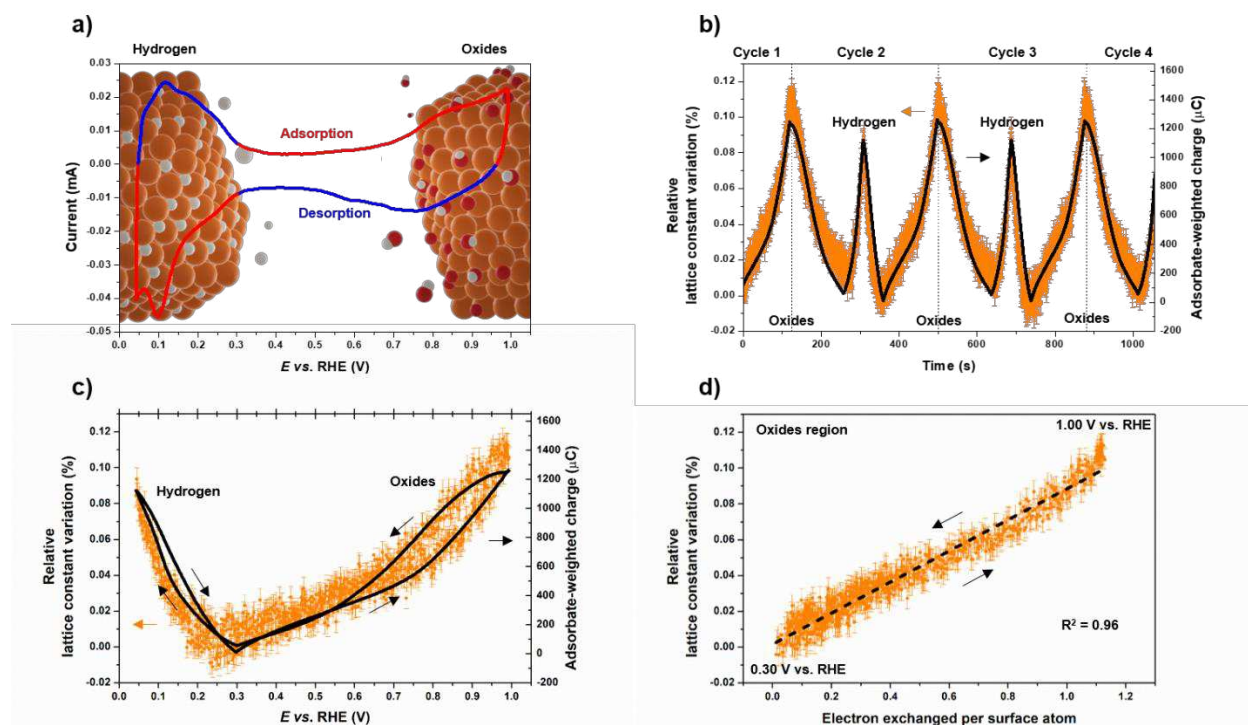


5

6 **Figure 3: Monitoring hydrogen absorption on Pd nanocatalyst:** (a) $\text{PdH}_x \alpha \leftrightarrow \beta$ phase transition lattice
 7 constants hysteresis at the steady state (square symbols interpolated by black lines) measured after 60 s hold at
 8 various potentials, superimposed with the data from cyclic voltammetry at 5 mV s^{-1} (circle symbols); b) evolution
 9 of coherent domain sizes as a function of time for the two phases transitions during cyclic voltammetry. In b) the
 10 deduced core-shell model evolution schematics for the phase transitions is presented, including the PdH_x - α
 11 (cyan), supersaturated PdH_x - α (dark cyan), undersaturated PdH_x - β (orange) and PdH_x - β (red) phases.

1

2 More insights into the phase transition mechanism can be provided by Rietveld refinement. **Figure 3.b**
3 shows an interesting evolution of the coherent domains sizes for the two phases: whereas the PdH_x- α
4 domain size follows an expected full range size decrease (increase) during PdH_x $\alpha \rightarrow \beta$ (PdH_x $\beta \rightarrow \alpha$) phase
5 transition, the amplitude variation of the domain size for PdH_x- β is much narrower. This suggests that the
6 core-shell evolution of the phase transitions observed in the gas phase for fine Pd nanoparticles (<10 nm)
7 ^{18,21} is also valid in electrochemical environment. The PdH_x- β -shell thickening (possibly interpreted as a
8 coherent hollow nanoparticle of decreasing inner void sizes) 'seen' as a solid particle of constant diameter
9 by the Rietveld analysis of the WAXS pattern is supported by Burresi *et al.* recent work ⁴¹. A slight increase
10 of the PdH_x- β size and slight growth of the PdH_x- α size are observed during the early stage of PdH_x $\alpha \rightarrow \beta$
11 transition. An excess of the PdH_x- β size appears only during PdH_x $\beta \rightarrow \alpha$ transition. This perfectly illustrates
12 the size-dependent transition kinetics of the nanoparticles composing the samples (see transmission electron
13 microscopy images and associated particles size distributions, **Figure S4**). As smaller particles complete
14 both transitions faster than large ones ¹⁸, the remaining volume-averaged size estimation provided by XRD
15 at a given time produces the observed asymmetric trends. **Figure 3.b** illustrates the present findings
16 regarding the PdH_x $\alpha \leftrightarrow \beta$ phase transition mechanism: the core-shell formation steps during absorption
17 (panels (i) to (v)) are found reversible for desorption (panels (v) to (ix)).



1
2 **Figure 4: Monitoring adsorption on Pt:** (a) cyclic voltammograms of Pt/C in N_2 -purged 0.1 M $HClO_4$ recorded
3 at room temperature with a potential sweep rate of 5 mV s^{-1} ; associated variations of the relative lattice constant
4 variation (orange) and adsorbate-weighted integrated charge (black) as a function of (b) time along several
5 potential cycles and (c) as a function of the potential for one cycle ; (d) relative lattice constant variations
6 (orange) measured as a function of the electron exchanged per surface atom with associated linear regression
7 (dash line). The weights associated to current integration were $+1$ for adsorption (red regions in (a)) and -1 for
8 desorption (blue regions in (a)). The signals are displayed as scatter points (377 ms resolution) and the error
9 bars represent the standard deviation associated with the refinement of the plotted parameters. The electrode
10 was loaded with $25\text{ }\mu\text{g}_{Pt}\text{ cm}^{-2}$ and the WAXS measured in grazing incidence configuration.

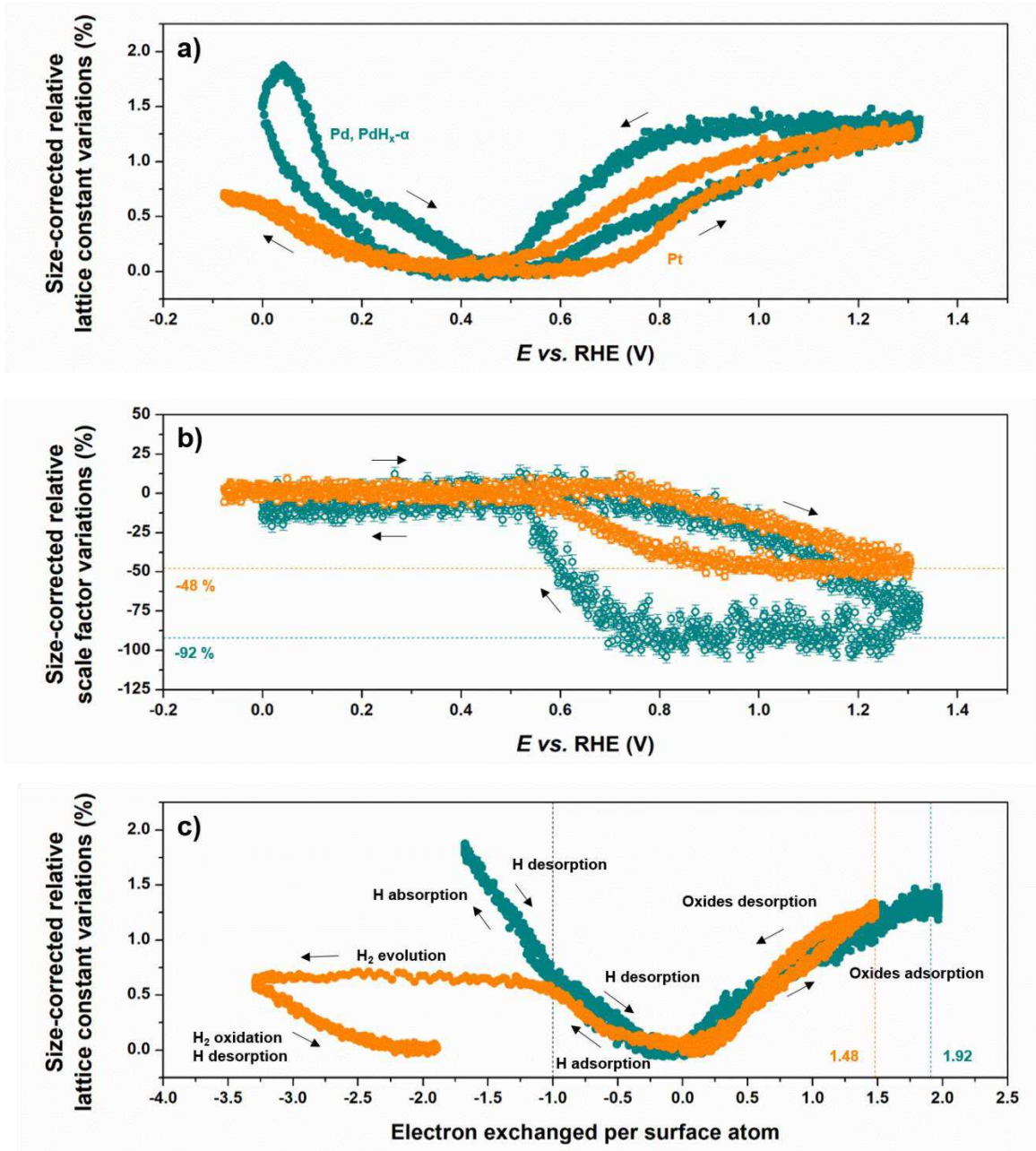
11
12 The enhanced surface-to-volume ratio of nanoparticles allows changes in the overall lattice constant of
13 crystalline nanoparticles upon adsorption processes to be measured ⁴², a largely-overlooked effect in
14 nanocatalysts studies. As investigated firstly by Nagy *et al.* ²³ on single crystal surfaces and by Martens *et*
15 *al.* ⁴³ and then by Schmieles *et al.* ⁴⁴ for Pt nanoparticles, XRD is a powerful tool to probe the dynamics of
16 surface-oxide formation *operando*. However, quantitative correlation between microstructural changes and

1 adsorbate surface coverage (reactivity descriptor) was still unachieved. **Figure 4.a** shows the cyclic
2 voltammogram of Pt/C nanoparticles in typical electrocatalysis laboratory conditions ($25 \mu\text{g}_{\text{Pt}} \text{cm}^{-2}$ thin-
3 film in N_2 -saturated 0.1 M HClO_4) recorded during *operando* WAXS. The potential window was kept
4 between 0.05 and 1.00 V vs. RHE to inhibit Faradaic hydrogen evolution and extensive Pt dissolution. To
5 compare the adsorbates surface coverage with the nanoparticles lattice constant, the current was integrated
6 by introducing a positive weight for adsorption (+1, red regions on the cyclic voltammogram) and a negative
7 weight for desorption (-1, blue regions of the cyclic voltammogram). Superimposing the integration results
8 with the relative lattice constant variation *versus* time (377 ms resolution) during consecutive potential
9 cycles (**Figure 4.b**) unambiguously reveals the strong correlation existing between adsorbate formation and
10 nanoparticle lattice expansion. Focusing on a single potential cycle (**Figure 4.c**), reveals a trend on
11 nanoparticles very close to model studies conducted on electrochemical quartz-crystal micro- or nano-
12 balances (EQCM, EQCN) ⁴⁵⁻⁴⁷. Especially, the lattice constant variation in the double layer region (~ 0.35
13 $- 0.55 \text{ V vs. RHE}$) measured here agrees with electrode mass increase from EQCM measurements in
14 HClO_4 electrolyte ⁴⁶, confirming that adsorption (OH , H_2O , ClO_4^- ²⁸) or displacement (between OH_{ads} and
15 H_{ads} ^{29,48}) processes occur in this region. Consequently, we chose to include the so-called double-layer
16 current in the integration. The question of how this double layer current seems to provide good
17 approximation of the adsorption or displacement processes (which may produce current or not) in this
18 particular region in light of the lattice constant changes would however require further investigations. By
19 using the common assumption of one hydrogen adsorbed per surface atom at full hydrogen coverage,
20 normalizing the electrical charge passed through the electrode by the one of the underpotentially-deposited
21 hydrogen region (H_{UPD}) allows us to represent the variation of the lattice constant as a function of electron
22 exchanged per surface atom in **Figure 4.d**. The plot shows a robust, unique linear trend for both potential
23 sweep directions. Thus, the nanoparticles lattice constant is an experimentally accessible structural
24 descriptor of their adsorption trend, whatever the potential and electrode history. Most importantly, this
25 descriptor can be measured directly during catalyst operation in electrochemical environment beyond
26 theoretical predictions. The chemical nature of the adsorbates is however not provided. Still, it can be

1 reasonably approximated that values of electron-exchanged-per-surface atoms correspond to oxidation
2 states, which gives information on possible adsorbates. Thus exchanged electron values below 1 likely
3 translate to θ_{OH} , the coverage of OH_{ads} .

4 The present results make clear that both absorption and adsorption processes contribute to nanoparticles
5 lattice expansion. Comparing trends on Pd and Pt in alkaline electrolyte (**Figure 5**) shows that these
6 processes, together with Faradaic reactions (such as hydrogen evolution), can still be distinguished from
7 each other. To clarify the comparison, however, the low potential vertex of the cyclic voltammetry was up-
8 shifted to 0.00 V vs. RHE for Pd to prevent the formation of the PdH_x - β phase (while hydrogen absorption
9 still occurs in PdH_x - α). **Figure 5.a** and **5.b** show the relative, size-corrected evolutions of the lattice
10 constants and scale factors, respectively, measured for the two materials during cyclic voltammetry. The
11 proposed correction from the size consists of dividing the raw parameters values by the dispersion (the
12 proportion of surface atoms, in %) and was found necessary when comparing two materials of different
13 particle sizes^{15,49} (correction details are provided in the Supplementary Information). In light of the lattice
14 constant changes, **Figure 5.a** makes clear that Pt features lower oxides surface coverage than Pd in the 0.60
15 $\leq E \leq 0.90$ V vs. RHE potential window in these experimental conditions. The size-corrected, relative scale
16 factor losses plotted in **Figure 5.b** can be directly interpreted as the fraction of the surface undergoing place
17 exchange amorphisation (in %). The value at 1.32 V vs. RHE is found higher for Pd (-92%), which results
18 in larger irreversibility during the negative-going potential scan compared to Pt (-48%). As previously
19 discussed, different lattice constant evolutions between Pd and Pt are observed during electrode polarization
20 below $E = 0.40$ V vs. RHE. Especially, from **Figure 5.a**, bulk hydrogen absorption is found to produce
21 more pronounced lattice constant expansion than surface adsorption. Finally, **Figure 5.c** shows the variation
22 of the lattice constants *versus* the number of electrons exchanged. Since the H_{UPD} region is not defined on
23 the cyclic voltammograms in these experimental conditions (H_2 evolution/oxidation on Pt and bulk
24 absorption/desorption on Pd), the values were estimated from the electrical charge passed at the slope break
25 in the lattice constant variation between hydrogen adsorption and either hydrogen evolution on Pt or

1 hydrogen absorption on Pd. These slope breaks consequently appear at the -1 electron-exchanged-per-
2 surface-atom line in **Figure 5.c**. Below this limit, Pt catalyzes the hydrogen evolution with constant lattice
3 expansion, whereas Pd undergoes hydrogen absorption. The viability of the approach consisting of
4 disentangling hydrogen adsorption from absorption and evolution from their impact on the lattice constant
5 evolution trends is shown by its consistent impact on the oxidation trends. In fact, such H_{UPD} estimation
6 leads to maximum electrons exchanged per surface atom very close to 1.48 for Pt and 1.92 for Pd (see
7 dashed-lines) during maximum oxidation. This translates into O_{ads} (2-electron process) surface coverages
8 of 0.48 and 0.92 for Pt and Pd (if the rest of the surface is covered by 1-electron process OH_{ads}), respectively.
9 These values are the ones found from the O_{ads} induced ²⁷ place-exchange amorphisation revealed by the
10 size-corrected relative scale factor losses in **Figure 5.b**. These convergent observations strongly support
11 the proposed disentanglement of the different electrochemical processes based on the feedback of their
12 distinct fingerprints on catalysts microstructures, as labeled in **Figure 5.c**.



1
 2 **Figure 5: Disentangling adsorption, absorption and Faradaic processes from their fingerprints on catalysts**
 3 **microstructure:** (a) Size-corrected relative lattice constant variation and (b) size-corrected scale factor
 4 variation for Pd/C and Pt/C catalysts as a function of electrode potential; (c) size-corrected lattice constant
 5 variation as a function of number of electron exchanged per surface atom during cyclic voltammetry in N₂-
 6 saturated 0.1 M NaOH. The signals are displayed as scatter points (333 ms time resolution) and the error bars
 7 represent the standard deviation associated with the refinement of the plotted parameters. The electrodes were
 8 loaded with 1.45 mg_{metal} cm⁻² and measured in transmission configuration.

1
2
3
4
5
6
7
8
9
10
11
12
13
14
15
16
17
18
19
20
21
22
23

In summary, we used the brilliance of the 4th generation ESRF-EBS light source to investigate the structures of device-relevant Pd and Pt nanocatalysts during cyclic voltammetry. When examined with this new light, nanocatalyst microstructural parameters measured *operando* are revealed with such fine resolution that insightful new information into the mechanism of their surface reactions can be deduced. Contrary to the central concept of the catalyst-by-design approach where the catalyst structure dictates its adsorption trend, the electrochemical environment has a ubiquitous, strong feedback on the catalyst structure. For nanocatalysts with enhanced surface-to-volume ratio, which are of primary importance for device applications, the surface-induced changes translate into modified bulk properties. Looking at Pd nanoparticles phase transitions during electrochemical hydrogen absorption allowed the first experimental detection of unstable transient states that were long-time predicted from mathematical models. Notably, a core-shell model mechanism in agreement with results from the gas phase could be proposed. Finally, we demonstrated that electrochemical adsorbates coverages can be quantified and distinguished from other processes from structural changes they generate on nanoparticles. Such facile experimental access to fundamental reactivity and stability descriptors *operando* is foreseen to provide a reliable path to further nanocatalyst development encompassing a wide range of applications. Above all, these results should serve to improve the current theoretical description of nanomaterials in practical environments.

1 *METHODS*

2 **Electrocatalysts**

3 For the Palladium experiment, a Pd/Vulcan XC72[®] catalyst with a Pd weight fraction (wt.%) of 20% was
4 purchased from Premetek and used as reference material without any treatment. For the Platinum
5 experiment in alkaline electrolyte, a Pt/Vulcan XC72[®] catalyst with a Pt weight fraction (wt.%) of 20%
6 (TEC10V20E) was purchased from Tanaka Kikinzoku Kogyo (TKK) and used as reference material
7 without any treatment. For the Platinum experiment in acidic electrolyte, a Pt/Vulcan XC72[®] catalyst with
8 a Pt weight fraction (wt.%) of 25% was prepared via wet impregnation followed by thermal reduction in
9 hydrogen atmosphere in a fluidized bed reactor as reported elsewhere⁵⁰ (for details see Supplementary
10 information).

11 **Electrochemical Measurements**

12 All the glassware accessories and cell components used in this study were firstly cleaned by soaking in a
13 H₂SO₄:H₂O₂ mixture for at least 12 hours and thoroughly washed in Milli-Q water (Millipore, 18.2 MΩ
14 cm, total organic compounds < 3 ppb). A Biologic potentiostat SP300 and custom-made three-electrode
15 electrochemical flow cells were used. The electrolyte (0.1 M NaOH, Suprapur[®], Merck or 0.1 M HClO₄,
16 Suprapur[®], Merck) was prepared prior each sample measurement and flowed constantly through the cell at
17 a rate of 20 mL min⁻¹ using a peristaltic pump. The counter-electrode was a Pt wire and the reference
18 electrode a commercial Hg/HgO electrode (OrygaLys) in case of Pd, and a commercial leakless miniature
19 Ag/AgCl electrode (ET072, eDAQ) in case of Pt.

20 To prepare the thin-film working electrodes for transmission geometry, 20 μL of a catalytic ink suspension
21 containing 2.3 g_{metal} L⁻¹ was pipetted and dried on a 16 mm diameter disk commercial gas diffusion
22 electrode (Freundenberg, WE-95-2SH). The diameter of the as-formed catalytic film was typically around
23 2 mm, corresponding to a metal loading of 1.45 mg_{metal} cm⁻². The ink suspensions were composed of 29

1 mg of catalyst powder (20 wt.% metal), 154 μL of 5 wt.% Nafion[®] solution (Electrochem. Inc.), 743 μL of
2 isopropanol and 1.8 mL (18.2 M Ω cm) of deionized water (MQ-grade, Millipore). For the grazing incidence
3 geometry, 10 μL of a catalytic ink suspension containing 0.49 $\text{g}_{\text{metal}} \text{L}^{-1}$ was pipetted and dried on a 5 mm
4 diameter mirror-polished glassy carbon cylinder, thus reaching a metal loading of 25 $\mu\text{g}_{\text{metal}} \text{cm}^{-2}$. The
5 ink suspensions were composed of 10 mg of catalyst powder (25 wt.% metal), 54 μL of 5 wt. % Nafion[®]
6 solution (Electrochem. Inc.), 1446 μL of isopropanol and 3.6 mL (18.2 M Ω cm) of deionized water (MQ-
7 grade, Millipore).

8 **Synchrotron Wide-Angle X-Ray Scattering (WAXS) Measurements**

9 Synchrotron WAXS measurements were performed at ID31 beamline of the European Synchrotron
10 Radiation facility (ESRF) in Grenoble, France. The high energy X-ray beam (78 keV) was focused on the
11 catalyst powders through the cells in transmission or grazing incidence modes, and the scattered signal was
12 collected using a Dectris Pilatus CdTe 2M detector positioned 850 mm behind the sample. The energy,
13 detector distance and tilts were calibrated using a standard CeO₂ powder and the 2D diffraction patterns
14 were reduced to the presented 1D curves using the pyFAI software package⁵¹.

15 **Rietveld Refinements**

16 Rietveld refinement of the WAXS patterns was performed to extract the phase structure, crystallite size,
17 lattice parameter and scale factor using the *Fm3m* structure of Pd and Pt metal and the Fullprof software.
18 The instrumental resolution function was determined by the refinement of a CeO₂ standard sample.
19 Thomson-Cox-Hastings profile function was adopted⁵². The background of patterns was described by an
20 interpolated set of points with refinable intensities.

21 **Data Availability.**

22 The datasets generated during and/or analysed during the current study are available from the corresponding
23 author on reasonable request.

1

2 REFERENCES

- 3 (1) Henry, C. R. Surface Studies of Supported Model Catalysts. *Surf. Sci. Rep.* **1998**, *31*, 231–325.
- 4 (2) Markovic, N. M.; Ross Jr., P. N. Surface Science Studies of Model Fuel Cell Electrocatalysts. *Surf.*
5 *Sci. Rep.* **2002**, *45* (4–6), 117–229.
- 6 (3) Nørskov, J. K.; Rossmeisl, J.; Logadottir, a.; Lindqvist, L.; Kitchin, J. R.; Bligaard, T.; Jónsson, H.
7 Origin of the Overpotential for Oxygen Reduction at a Fuel-Cell Cathode. *J. Phys. Chem. B* **2004**,
8 *108* (46), 17886–17892.
- 9 (4) Jiao, Y.; Zheng, Y.; Jaroniec, M.; Qiao, S. Z. Design of Electrocatalysts for Oxygen- and Hydrogen-
10 Involving Energy Conversion Reactions. *Chem. Soc. Rev.* **2015**, *44* (8), 2060–2086.
- 11 (5) Nørskov, J. K.; Bligaard, T.; Rossmeisl, J.; Christensen, C. H. Towards the Computational Design
12 of Solid Catalysts. *Nat. Chem.* **2009**, *1* (1), 37–46.
- 13 (6) Hammes-Schiffer, S. Catalysts by Design: The Power of Theory. *Acc. Chem. Res.* **2017**, *50* (3),
14 561–566.
- 15 (7) Zhao, Z.; Liu, S.; Zha, S.; Cheng, D.; Studt, F.; Henkelman, G.; Gong, J. Theory-Guided Design of
16 Catalytic Materials Using Scaling Relationships and Reactivity Descriptors. *Nat. Rev. Mater.* **2019**,
17 *4*, 792–804.
- 18 (8) Mistry, H.; Varela, A. S.; Kühl, S.; Strasser, P.; Cuenya, B. R. Nanostructured Electrocatalysts with
19 Tunable Activity and Selectivity. *Nat. Rev. Mater.* **2016**, *1* (4), 16009.
- 20 (9) Calle-Vallejo, F.; Koper, M. T. M.; Bandarenka, A. S. Tailoring the Catalytic Activity of Electrodes
21 with Monolayer Amounts of Foreign Metals. *Chem. Soc. Rev.* **2013**, *42* (12), 5210–5230.
- 22 (10) Stephens, I. E. L.; Rossmeisl, J.; Chorkendorff, I. Toward Sustainable Fuel Cells. *Science* **2016**, *354*
23 (6318), 1378–1379.
- 24 (11) Calle-Vallejo, F.; Pohl, M. D.; Reinisch, D.; Loffreda, D.; Sautet, P.; Bandarenka, A. S. Why
25 Conclusions from Platinum Model Surfaces Do Not Necessarily Lead to Enhanced Nanoparticle
26 Catalysts for the Oxygen Reduction Reaction. *Chem. Sci.* **2017**, *8* (3), 2283–2289.
- 27 (12) Ruiz-Zepeda, F.; Gatalo, M.; Pavlišić, A.; Dražić, G.; Jovanović, P.; Bele, M.; Gaberšček, M.;
28 Hodnik, N. Atomically Resolved Anisotropic Electrochemical Shaping of Nano-Electrocatalyst.
29 *Nano Lett.* **2019**, *19* (8), 4919–4927.
- 30 (13) Cui, C.; Gan, L.; Heggen, M.; Rudi, S.; Strasser, P. Compositional Segregation in Shaped Pt Alloy
31 Nanoparticles and Their Structural Behaviour during Electrocatalysis. *Nat. Mater.* **2013**, *12* (8),
32 765–771.
- 33 (14) Cherevko, S.; Kulyk, N.; Mayrhofer, K. J. J. Durability of Platinum-Based Fuel Cell
34 Electrocatalysts: Dissolution of Bulk and Nanoscale Platinum. *Nano Energy* **2016**, *29*, 275–298.
- 35 (15) Chattot, R.; Bacq, O. Le; Beermann, V.; Kühl, S.; Herranz, J.; Henning, S.; Kühn, L.; Asset, T.;

- 1 Guétaz, L.; Renou, G.; et al. Surface Distortion as a Unifying Concept and Descriptor in Oxygen
2 Reduction Reaction Electrocatalysis. *Nat. Mater.* **2018**, *17* (9), 827–833.
- 3 (16) Bergmann, A.; Roldan Cuenya, B. Operando Insights into Nanoparticle Transformations during
4 Catalysis. *ACS Catal.* **2019**, *9* (11), 10020–10043.
- 5 (17) Eastman, J. A.; Thompson, L. J.; Kestel, B. J. Narrowing of the Palladium-Hydrogen Miscibility
6 Gap in Nanocrystalline Palladium. *Phys. Rev. B* **1993**, *48* (1), 84–93.
- 7 (18) Langhammer, C.; Zhdanov, V. P.; Zorić, I.; Kasemo, B. Size-Dependent Kinetics of Hydriding and
8 Dehydriding of Pd Nanoparticles. *Phys. Rev. Lett.* **2010**, *104* (13), 2–5.
- 9 (19) Syrenova, S.; Wadell, C.; Nugroho, F. A. A.; Gschneidner, T. A.; Diaz Fernandez, Y. A.; Nalin,
10 G.; Świtlik, D.; Westerlund, F.; Antosiewicz, T. J.; Zhdanov, V. P.; et al. Hydride Formation
11 Thermodynamics and Hysteresis in Individual Pd Nanocrystals with Different Size and Shape. *Nat.*
12 *Mater.* **2015**, *14* (12), 1236–1244.
- 13 (20) Baldi, A.; Narayan, T. C.; Koh, A. L.; Dionne, J. A. In Situ Detection of Hydrogen-Induced Phase
14 Transitions in Individual Palladium Nanocrystals. *Nat. Mater.* **2014**, *13* (12), 1143–1148.
- 15 (21) Bugaev, A. L.; Guda, A. A.; Lomachenko, K. A.; Shapovalov, V. V.; Lazzarini, A.; Vitillo, J. G.;
16 Bugaev, L. A.; Groppo, E.; Pellegrini, R.; Soldatov, A. V.; et al. Core-Shell Structure of Palladium
17 Hydride Nanoparticles Revealed by Combined X-Ray Absorption Spectroscopy and X-Ray
18 Diffraction. *J. Phys. Chem. C* **2017**, *121* (33), 18202–18213.
- 19 (22) Jerkiewicz, G. Hydrogen Sorption at/in Electrodes. *Prog. Surf. Sci.* **1998**, *57* (2), 137–186.
- 20 (23) Nagy, Z.; You, H. Applications of Surface X-Ray Scattering to Electrochemistry Problems.
21 *Electrochim. Acta* **2002**, *47* (19), 3037–3055.
- 22 (24) Topalov, A. A.; Cherevko, S.; Zeradjanin, A. R.; Meier, J. C.; Katsounaros, I.; Mayrhofer, K. J. J.
23 Towards a Comprehensive Understanding of Platinum Dissolution in Acidic Media. *Chem. Sci.*
24 **2014**, *5* (2), 631–638.
- 25 (25) Ruge, M.; Drnec, J.; Rahn, B.; Reikowski, F.; Harrington, D. A.; Carlà, F.; Felici, R.; Stettner, J.;
26 Magnussen, O. M. Structural Reorganization of Pt(111) Electrodes by Electrochemical Oxidation
27 and Reduction. *J. Am. Chem. Soc.* **2017**, *139* (12), 4532–4539.
- 28 (26) Drnec, J.; Ruge, M.; Reikowski, F.; Rahn, B.; Carlà, F.; Felici, R.; Stettner, J.; Magnussen, O. M.;
29 Harrington, D. A. Initial Stages of Pt(111) Electrooxidation: Dynamic and Structural Studies by
30 Surface X-Ray Diffraction. *Electrochim. Acta* **2017**, *224*, 220–227.
- 31 (27) Fuchs, T.; Drnec, J.; Calle-Vallejo, F.; Stubb, N.; Sandbeck, D. J. S.; Ruge, M.; Cherevko, S.;
32 Harrington, D. A.; Magnussen, O. M. Structure Dependency of the Atomic-Scale Mechanisms of
33 Platinum Electro-Oxidation and Dissolution. *Nat. Catal.* **2020**, *3* (9), 754–761.
- 34 (28) Kondo, T.; Masuda, T.; Aoki, N.; Uosaki, K. Potential-Dependent Structures and Potential-Induced
35 Structure Changes at Pt(111) Single-Crystal Electrode/Sulfuric and Perchloric Acid Interfaces in the
36 Potential Region between Hydrogen Underpotential Deposition and Surface Oxide Formation by in
37 Situ Su. *J. Phys. Chem. C* **2016**, *120* (29), 16118–16131.

- 1 (29) Huang, Y. F.; Kooyman, P. J.; Koper, M. T. M. Intermediate Stages of Electrochemical Oxidation
2 of Single-Crystalline Platinum Revealed by in Situ Raman Spectroscopy. *Nat. Commun.* **2016**, *7*,
3 1–7.
- 4 (30) Merte, L. R.; Behafarid, F.; Miller, D. J.; Friebel, D.; Cho, S.; Mbuga, F.; Sokaras, D.; Alonso-Mori,
5 R.; Weng, T. C.; Nordlund, D.; et al. Electrochemical Oxidation of Size-Selected Pt Nanoparticles
6 Studied Using in Situ High-Energy-Resolution X-Ray Absorption Spectroscopy. *ACS Catal.* **2012**,
7 *2* (11), 2371–2376.
- 8 (31) Sasaki, K.; Marinkovic, N.; Isaacs, H. S.; Adzic, R. R. Synchrotron-Based in Situ Characterization
9 of Carbon-Supported Platinum and Platinum Monolayer Electrocatalysts. *ACS Catal.* **2016**, *6* (1),
10 69–76.
- 11 (32) Martens, I.; Chattot, R.; Rasola, M.; Blanco, M. V.; Honkimäki, V.; Bizzotto, D.; Wilkinson, D. P.;
12 Drnec, J. Probing the Dynamics of Platinum Surface Oxides in Fuel Cell Catalyst Layers Using in
13 Situ X-Ray Diffraction. *ACS Appl. Energy Mater.* **2019**, *2* (11), 7772–7780.
- 14 (33) Lewis, F. A. The Hydrides of Palladium and Palladium Alloys. *Platin. Met. Rev.* **1960**, *4* (4), 132–
15 137.
- 16 (34) Lewis, F. A. The Palladium-Hydrogen System: Structures near Phase Transition and Critical Points.
17 *Int. J. Hydrogen Energy* **1995**, *20* (7), 587–592.
- 18 (35) Scholtus, N. A.; Keith Hall, W. Hysteresis in the Palladium-Hydrogen System. *J. Chem. Phys.* **1962**,
19 *39* (4), 868–870.
- 20 (36) Lacher, J. R. A Theoretical Formula for the Solubility of Hydrogen in Palladium. *Proc. R. Soc.*
21 *London. Ser. A* **1937**, *161* (907), 525–545.
- 22 (37) Schwarz, R. B.; Khachatryan, A. G. Thermodynamics of Open Two-Phase Systems with Coherent
23 Interfaces. *Phys. Rev. Lett.* **1995**, *74* (13), 2523–2526.
- 24 (38) Schwarz, R. B.; Khachatryan, A. G. Thermodynamics of Open Two-Phase Systems with Coherent
25 Interfaces: Application to Metal-Hydrogen Systems. *Acta Mater.* **2006**, *54* (2), 313–323.
- 26 (39) Johnson, N. J. J.; Lam, B.; MacLeod, B. P.; Sherbo, R. S.; Moreno-Gonzalez, M.; Fork, D. K.;
27 Berlinguette, C. P. Facets and Vertices Regulate Hydrogen Uptake and Release in Palladium
28 Nanocrystals. *Nat. Mater.* **2019**, *18* (5), 454–458.
- 29 (40) Czerwinski, A.; Marassi, R. The Absorption of Hydrogen and Deuterium in Thin Palladium
30 Electrodes. Part II: Basic Solutions. *J. Electroanal. Chem.* **1992**, *322* (1–2), 373–381.
- 31 (41) Burrelli, E.; Tapfer, L. Diffraction Line Profiles of Spherical Hollow Nanocrystals. *Nanomater.*
32 *Nanotechnol.* **2019**, *9*, 1–11.
- 33 (42) Prieur, D.; Bonani, W.; Popa, K.; Walter, O.; Kriegsman, K. W.; Engelhard, M. H.; Guo, X.; Eloirdi,
34 R.; Gouder, T.; Beck, A.; et al. Size Dependence of Lattice Parameter and Electronic Structure in
35 CeO₂ Nanoparticles. *Inorg. Chem.* **2020**, *59* (8), 5760–5767.
- 36 (43) Martens, I.; Chattot, R.; Rasola, M.; Blanco, M. V.; Honkimäki, V.; Bizzotto, D.; Wilkinson, D. P.;
37 Drnec, J. Probing the Dynamics of Platinum Surface Oxides in Fuel Cell Catalyst Layers Using in

- 1 Situ X-Ray Diffraction. *ACS Appl. Energy Mater.* **2019**.
- 2 (44) Schmies, H.; Bergmann, A.; Hornberger, E.; Drnec, J.; Wang, G.; Dionigi, F.; Kühl, S.; Sandbeck,
3 D. J. S.; Mayrhofer, K. J. J.; Ramani, V.; et al. Anisotropy of Pt Nanoparticles on Carbon- And
4 Oxide-Support and Their Structural Response to Electrochemical Oxidation Probed by- And Situ
5 Techniques. *Phys. Chem. Chem. Phys.* **2020**, *22* (39), 22260–22270.
- 6 (45) Gloaguen, F.; Léger, J. M.; Lamy, C. Electrochemical Quartz Crystal Microbalance Study of the
7 Hydrogen Underpotential Deposition at a Pt Electrode. *J. Electroanal. Chem.* **1999**, *467* (1), 186–
8 192.
- 9 (46) Santos, M. C.; Miwa, D. W.; Machado, S. A. S. Study of Anion Adsorption on Polycrystalline Pt
10 by Electrochemical Quartz Crystal Microbalance. *Electrochem. commun.* **2000**, *2* (10), 692–696.
- 11 (47) Jerkiewicz, G.; Vatankhah, G.; Lessard, J.; Soriaga, M. P.; Park, Y. S. Surface-Oxide Growth at
12 Platinum Electrodes in Aqueous H₂SO₄ Reexamination of Its Mechanism through Combined
13 Cyclic-Voltammetry, Electrochemical Quartz-Crystal Nanobalance, and Auger Electron
14 Spectroscopy Measurements. *Electrochim. Acta* **2004**, *49* (9–10), 1451–1459.
- 15 (48) Chattot, R.; Martens, I.; Scohy, M.; Herranz, J.; Drnec, J.; Maillard, F.; Dubau, L. Disclosing Pt-
16 Bimetallic Alloy Nanoparticle Surface Lattice Distortion with Electrochemical Probes. *ACS Energy*
17 *Lett.* **2020**, *5* (1), 162–169.
- 18 (49) Chattot, R.; Asset, T.; Bordet, P.; Drnec, J.; Dubau, L.; Maillard, F. Beyond Strain and Ligand
19 Effects: Microstrain-Induced Enhancement of the Oxygen Reduction Reaction Kinetics on Various
20 PtNi/C Nanostructures. *ACS Catal.* **2017**, *7*, 398–408.
- 21 (50) Hornberger, E.; Schmies, H.; Paul, B.; Kühl, S.; Strasser, P. Design and Validation of a Fluidized
22 Bed Catalyst Reduction Reactor for the Synthesis of Well-Dispersed Nanoparticle Ensembles. *J.*
23 *Electrochem. Soc.* **2020**, *167* (11), 114509.
- 24 (51) Ashiotis, G.; Deschildre, A.; Nawaz, Z.; Wright, J. P.; Karkoulis, D.; Picca, F. E.; Kieffer, J. The
25 Fast Azimuthal Integration Python Library: PyFAI. *J. Appl. Crystallogr.* **2015**, *48*, 510–519.
- 26 (52) Thompson, P.; Cox, D. E.; Hastings, J. B. Rietveld Refinement of Debye-Scherrer Synchrotron X-
27 Ray Data from A1203. *J. Appl. Crystallogr.* **1987**, *20* (2), 79–83.

28

29 AUTHOR INFORMATION

30 Corresponding Author

31 * E-mail address for R.C: raphael.chattot@grenoble-inp.org

32 Author Contributions

1 R.C., M.C., and J.D. conceived the experiments, R.C., I.M., M.M. and M.R. performed the X-ray diffraction
2 experiments, F.R. and H.I.H. contributed to beamline operation, G.B. and E.H. synthesized the samples,
3 R.C. and M.C. did the electron microscopy, J.D., M.C., E.S, P.S and V.H. supervised the work. R.C.
4 analysed the data and wrote the first version of the manuscript. All authors discussed and approved the final
5 version of this manuscript.

6 Funding Sources

7 G.B, E.S and M.C. received financial support from the French National Research Agency (ANR, grant #
8 ANR-16-CE05-0009-01) in the frame of the MobiDiC project.

9 E.H. and P.S. received financial support from the German Federal Ministry of Education and Research
10 through grant 03XP0251 (“KorrZellKat”).

11

12

Figures

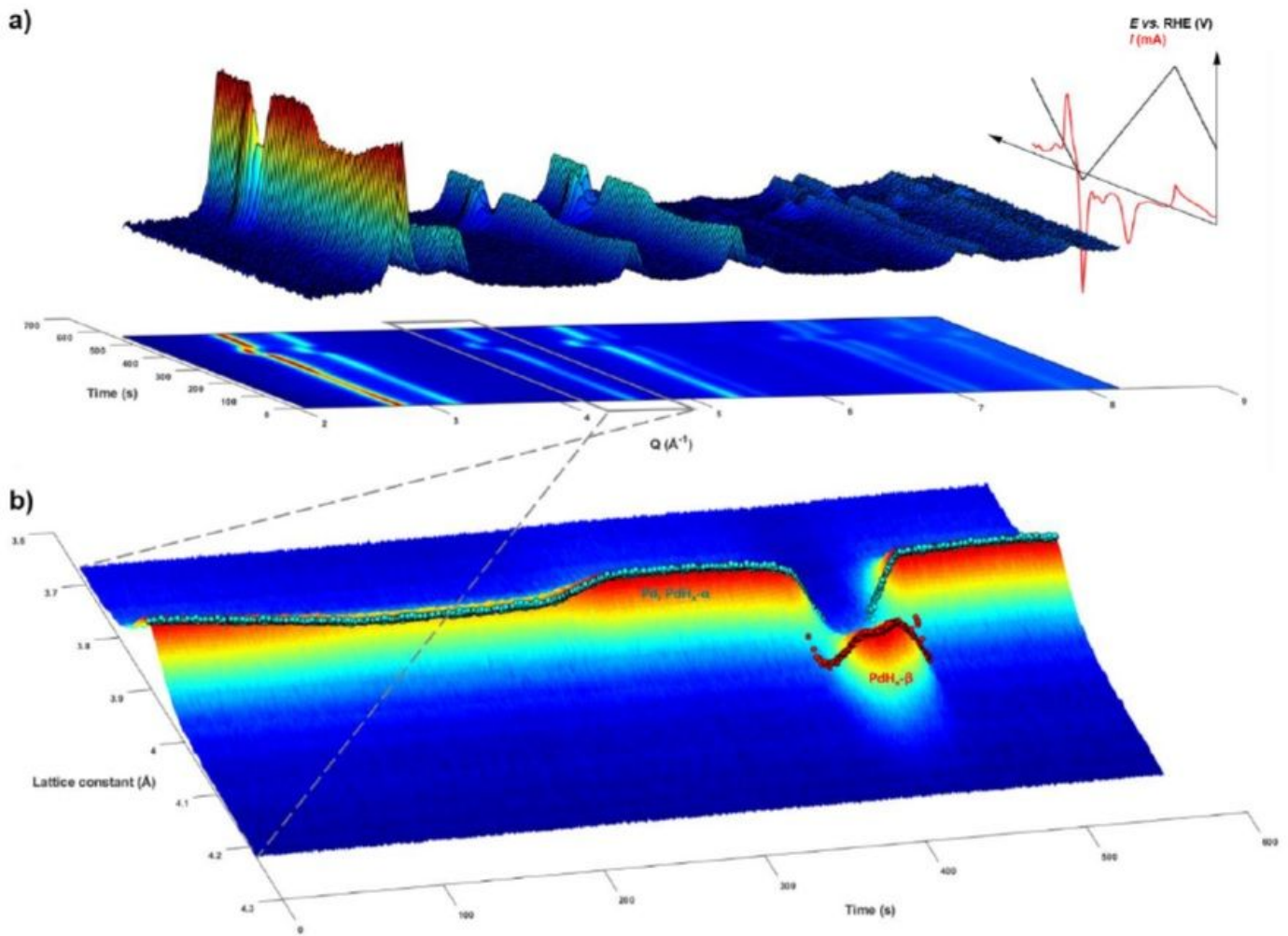


Figure 1

New light on Pd nanoparticles during cyclic voltammetry. a) 3D representation and corresponding 2D projection of WAXS patterns intensities (1 over 20) plotted as a function of time and the momentum transfer Q recorded during Pd cyclic voltammetry experiment in N_2 -purged 0.1 M NaOH electrolyte at room temperature. The evolutions of the electrochemical potential applied and measured electric current are also represented on the same time scale; b) surface plot focus on a narrow Q window showing the full time resolution evolution of the two phases (Pd, or PdH $_{x-\alpha}$ and PdH $_{x-\beta}$) [220] reflections. In b), the Q scale (left) is converted to the corresponding lattice constants, and the values calculated by Rietveld refinement of the full patterns are plotted on the surface of the plot. The exposure time for WAXS measurement was 250 ms, leading to an overall temporal resolution of 333 ms. The electrode was loaded with 1.45 $\mu\text{mol cm}^{-2}$ and the sweep rate was 5 mV s $^{-1}$.

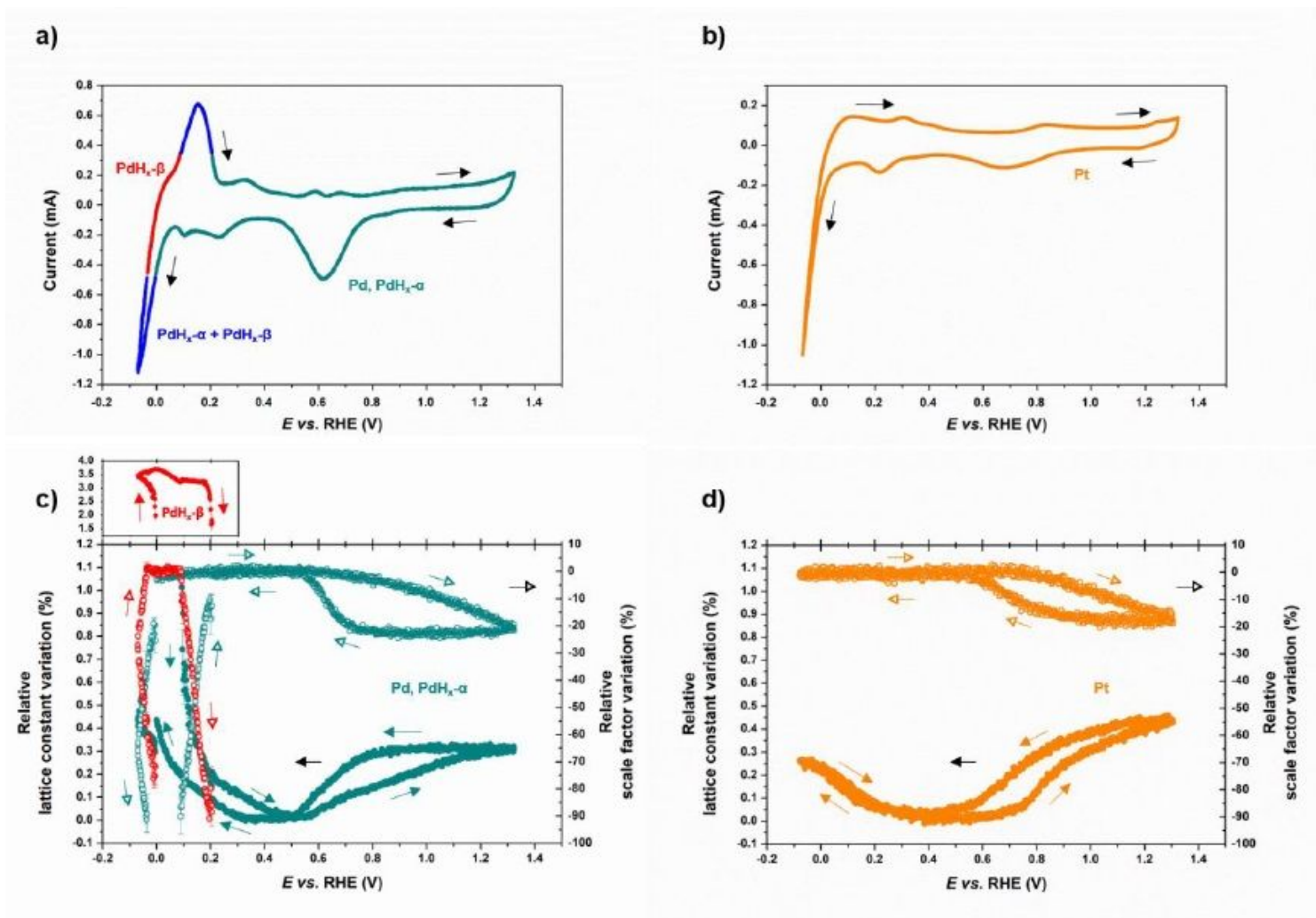


Figure 2

High time resolution monitoring of nanocatalysts microstructures during cyclic voltammetry. Cyclic voltammogram of the (a) Pd/C and (b) Pt/C catalysts in N₂-purged 0.1 M NaOH recorded at room temperature with a potential sweep rate of 5 mV s⁻¹; potential-dependency of the relative lattice constant variation (filled symbols, left axis) and relative scale factor (Bragg peaks area) variation (hollow symbols, right axis) for the (c) Pd/C and (d) Pt/C catalysts. In a), the current recorded in the potential regions is colored in cyan when only the phase Pd or PdH_x-α is detected, in red when only the PdH_x-β is detected and in blue when both PdH_x-α and PdH_x-β are detected simultaneously. In c) the signal colored in cyan corresponds to the Pd or PdH_x-α phase and the signal colored in red corresponds to the PdH_x-β phase. For the sake of clarity, the relative lattice constant variation of PdH_x-β phase is represented in a separated plot with linked x-axis. In all panels, the signals are displayed as scatter points (333 ms time resolution) and the error bars represent the standard deviation associated with the refinement of the plotted parameters. The electrodes were loaded with 1.45 μg cm⁻² and measured in transmission configuration.

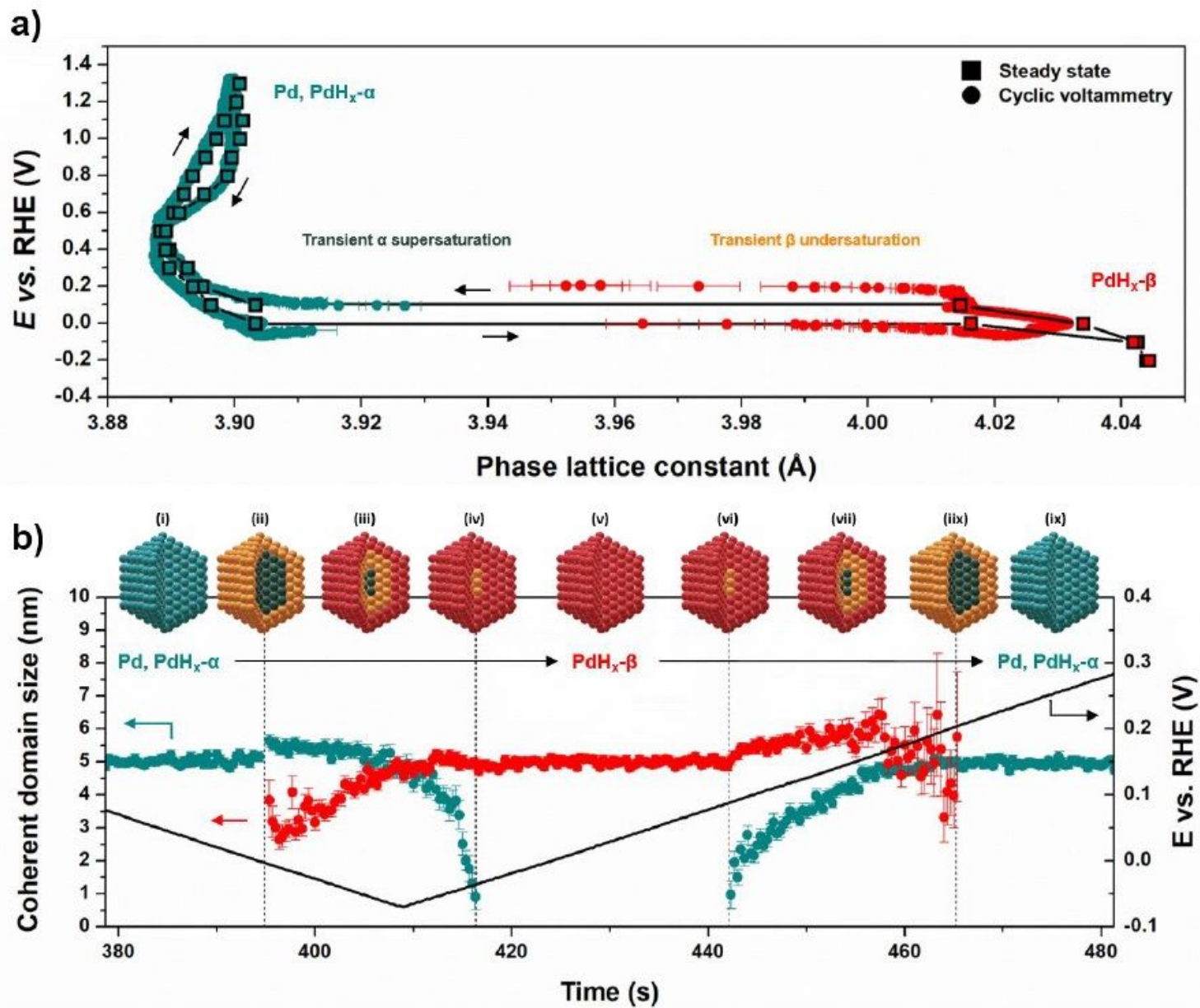


Figure 3

Monitoring hydrogen absorption on Pd nanocatalyst: (a) PdH_x phase transition lattice constants hysteresis at the steady state (square symbols interpolated by black lines) measured after 60 s hold at various potentials, superimposed with the data from cyclic voltammetry at 5 mV s⁻¹ (circle symbols); b) evolution of coherent domain sizes as a function of time for the two phase transitions during cyclic voltammetry. In b) the deduced core-shell model evolution schematics for the phase transitions is presented, including the PdH_x- α (cyan), supersaturated PdH_x- α (dark cyan), undersaturated PdH_x- α (orange) and PdH_x- β (red) phases.

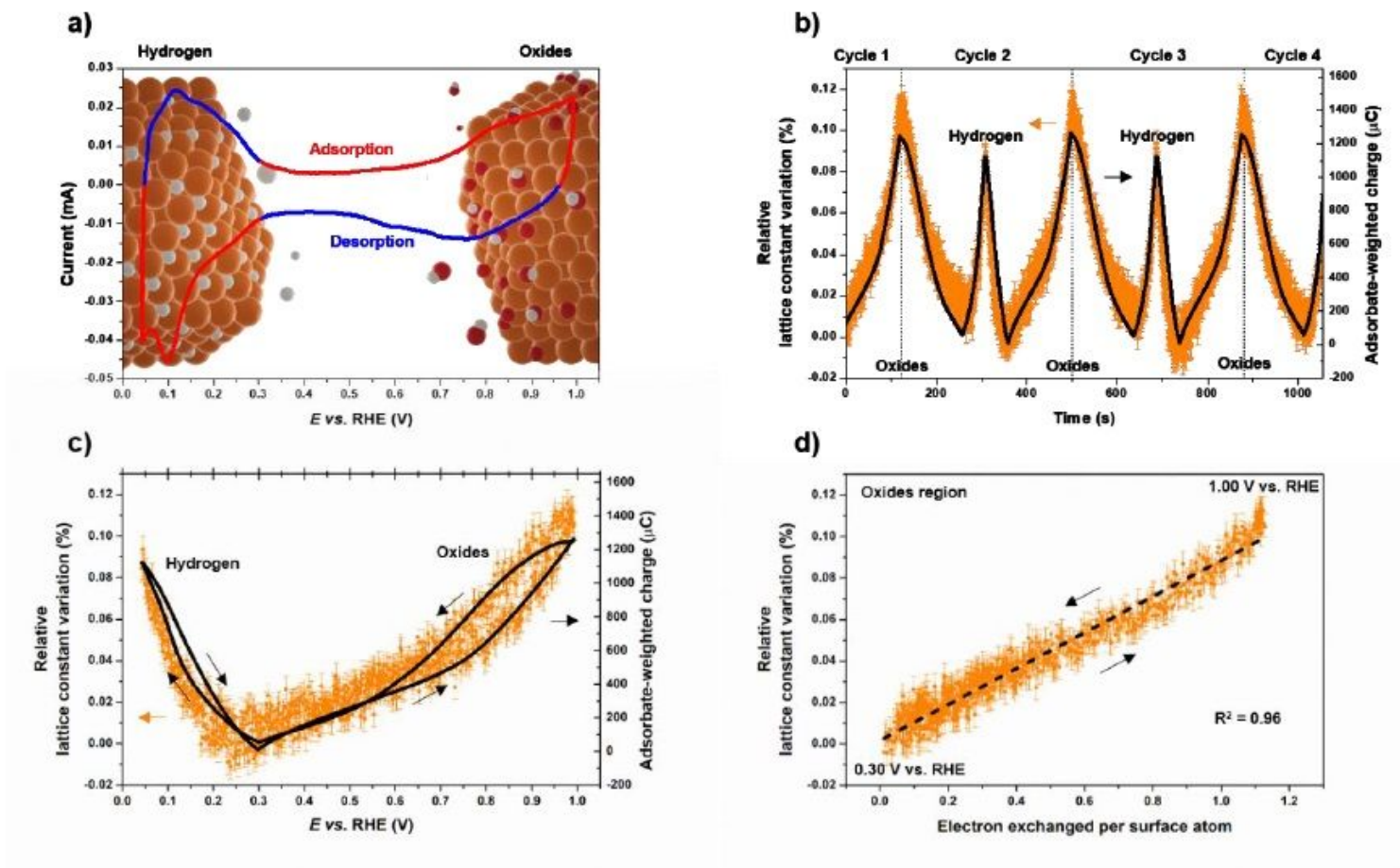


Figure 4

(a) cyclic voltammograms of Pt/C in N₂-purged 0.1 M HClO₄ recorded at room temperature with a potential sweep rate of 5 mV s⁻¹; associated variations of the relative lattice constant variation (orange) and adsorbate-weighted integrated charge (black) as a function of (b) time along several potential cycles and (c) as a function of the potential for one cycle; (d) relative lattice constant variations (orange) measured as a function of the electron exchanged per surface atom with associated linear regression (dash line). The weights associated to current integration were +1 for adsorption (red regions in (a)) and -1 for desorption (blue regions in (a)). The signals are displayed as scatter points (377 ms resolution) and the error bars represent the standard deviation associated with the refinement of the plotted parameters. The electrode was loaded with 25 μg Pt and the WAXS measured in grazing incidence configuration.

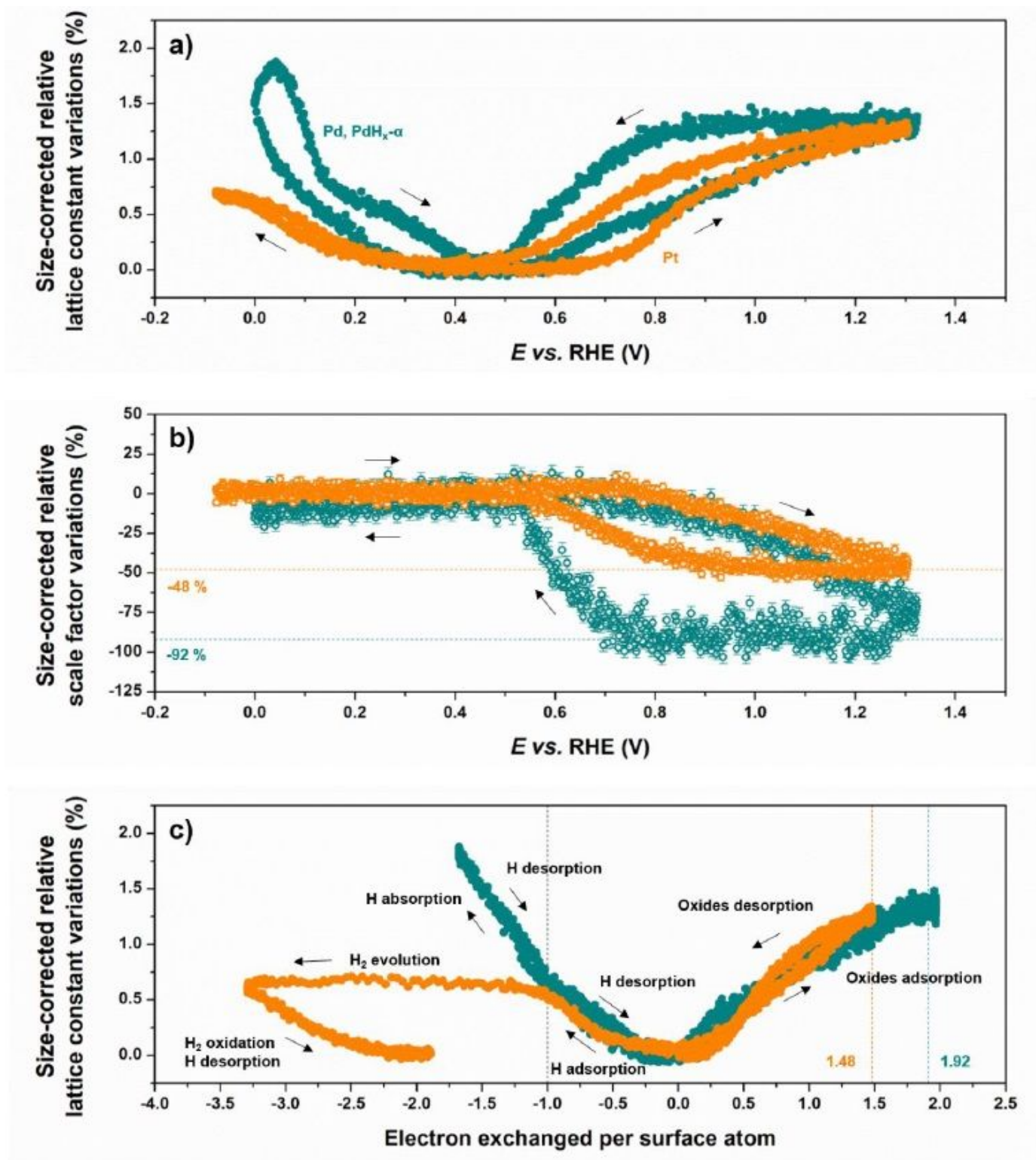


Figure 5

Disentangling adsorption, absorption and Faradaic processes from their fingerprints on catalysts microstructure: (a) Size-corrected relative lattice constant variation and (b) size-corrected scale factor variation for Pd/C and Pt/C catalysts as a function of electrode potential; (c) size-corrected lattice constant variation as a function of number of electron exchanged per surface atom during cyclic voltammetry in N₂-saturated 0.1 M NaOH. The signals are displayed as scatter points (333 ms time

resolution) and the error bars represent the standard deviation associated with the refinement of the plotted parameters. The electrodes were loaded with 1.45 $\mu\text{mol cm}^{-2}$ and measured in transmission configuration.

Supplementary Files

This is a list of supplementary files associated with this preprint. Click to download.

- [ElectrochemicalFeedbackSI.pdf](#)